

Compact Polarized X-Ray Source Based on All-Optical Inverse Compton Scattering

Yue Ma,^{1,2} Jianfei Hua^{1,*}, Dexiang Liu¹, Yunxiao He¹, Tianliang Zhang,¹ Jiucheng Chen,¹ Fan Yang,¹ Xiaonan Ning,¹ Hongze Zhang,¹ Yingchao Du,¹ and Wei Lu^{1,3,†}

¹*Department of Engineering Physics, Tsinghua University, Beijing 100084, China*

²*Institute of High Energy Physics, Chinese Academy of Sciences, Beijing 100049, China*

³*Beijing Academy of Quantum Information Sciences, Beijing 100193, China*



(Received 22 February 2022; revised 19 October 2022; accepted 15 December 2022; published 31 January 2023)

Polarized x-ray source is a useful probe for many fields, such as fluorescence imaging, magnetic microscopy, and nuclear physics research. All-optical inverse Compton scattering source (AOCS) based on a laser wakefield accelerator (LWFA) has drawn great attention in recent years due to its compact scale and high performance, especially its potential to generate polarized x rays. Here, polarization-tunable AOCS x rays are generated by a plasma-mirror-based scheme. The linearly and circularly polarized AOCS x rays are measured to have the mean photon energy of $60(\pm 5)/64(\pm 3)$ keV and the single-shot photon yield of approximately $1.1/1.3 \times 10^7$. A Compton polarimeter is designed to diagnose the x-ray polarization states, demonstrating the polarization tunability of AOCS, and indicating that the average polarization degree of the linearly polarized AOCS is $75(\pm 3)\%$ within 18.2 mrad x-ray divergence.

DOI: [10.1103/PhysRevApplied.19.014073](https://doi.org/10.1103/PhysRevApplied.19.014073)

I. INTRODUCTION

Polarized x-ray source has applications in widespread fields, particularly in fluorescence imaging [1,2], magnetic microscopy [3,4], and nuclear physics research [5,6]. For example, the utilization of a linearly polarized x-ray source in fluorescence imaging can significantly improve the image quality since the Compton photon background can be greatly suppressed in the x-ray polarization direction [1,2]. The left- and right-circularly polarized x rays have relatively different transmission in magnetic materials (magnetic circular dichroism) [3], which is the theoretical foundation of the magnetic microscopy [3,4].

Polarized x-ray photons are usually generated on the synchrotron radiation, x-ray free-electron laser (FEL), bremsstrahlung radiation, and inverse Compton scattering systems. Among these mechanisms, synchrotron radiation [7,8], and x-ray FEL [9,10] can produce ultrabright monoenergetic polarization-tunable x rays by inserting different kinds of undulators, and their polarization degree can access 100%. However, they are typically large-scale facilities and can hardly achieve high photon energy (<100 keV). Bremsstrahlung x rays are typically nonpolarized, while linearly polarized x rays can be generated at large observation angle by utilizing a thin target [11,12], and circularly polarized x rays can also be generated using

longitudinally polarized incident electrons [13]. However, these photons are typically partially polarized and the polarization adjustment is quite complicated. Inverse Compton scattering can produce keV-MeV quasimonoenergetic x rays with nearly 100% polarization degree, and the polarization state can be easily adjusted by tuning the polarization state of the scattering laser, showing distinct advantages in practical applications [14–16].

The laser wakefield accelerator (LWFA) [17–21] can generate MeV-GeV electron beams on a tabletop due to its ultrahigh acceleration gradient about 3 orders of magnitude higher than that of conventional accelerators. The inverse Compton-scattering source based on LWFA, termed the all-optical inverse Compton-scattering source (AOCS) [22–26], has drawn great attention due to its excellent performance (tunable polarization, tunable photon energy, quasimonoenergetic bandwidth), and benchtop scale. To date, several experiments about the optimization and the imaging applications of AOCS are reported, while its polarization characteristics have not been experimentally demonstrated.

In this paper, the generation of polarization-tunable AOCS x rays is demonstrated using a plasma-mirror-based scheme [25,26]. During the experiment, the drive laser of LWFA is reflected by a plasma mirror to scatter with the energetic LWFA electron beam, thus both the temporal and spatial synchronization of the electrons with the scattering lasers can be easily realized. Since the AOCS x rays near the axis duplicate the polarization of the scattering

*jfhua@tsinghua.edu.cn

†weilu@tsinghua.edu.cn

laser [15], the on-axis x rays have the highest polarization degree up to 100%, and the polarization state can be adjusted by tuning the polarization of the scattering laser. A dedicated Compton polarimeter [27–29] is designed to diagnose the polarization states of the AOCS x rays, showing good accordance with the simulation results.

II. GENERATION OF POLARIZED AOCS

The experiment is performed on the 10-TW Ti:sapphire laser system at Tsinghua University [30], and the setup is sketched in Fig. 1. Intense ultrashort laser pulses (800-nm wavelength, 500-mJ pulse energy, 40-fs pulse duration) are focused to a FWHM spot size of 9 μm on the leading edge of a 2-mm-diameter gas jet by an $f/18$ off-axis parabolic mirror (OAP), and 32.5% of the pulse energy is enclosed within the FWHM spot size. A quarter-wave plate with 50-mm diameter is inserted upstream of the OAP to adjust the laser polarization by tuning the wave-plate angle (angle between the optical axis of the quarter-wave plate and the polarization direction of the incident laser pulse), as shown in Fig. 1(a). When a laser pulse passes through the mixed gas (99.5% He + 0.5% N₂) ejected from the gas jet, plasma with density of about $1 \times 10^{19} \text{ cm}^{-3}$ is generated by laser ionization, and the plasma wakefield is formed behind the laser pulse. A mass of electrons is then injected into the acceleration phase of the wakefield and accelerated continuously to high energy. To measure the spectrum of the electron beam, a dipole magnet with 1-T magnetic field is inserted in the beam path. The single-shot spectra for continuous 35-shot electron beams driven by laser pulses with different polarization states are shown in Fig. 2(a), indicating that stable electron beams are generated using all these polarized lasers. For the linearly and circularly polarized drive lasers, the generated electron beams have the FWHM divergences of approximately 17/13 mrad (horizontal and vertical) and 18/16 mrad, respectively; the charges of 52 pC (36% RMS) and 74 pC (36% RMS), respectively. The corresponding accumulated spectra for continuous 50-shot electron beams are shown in Fig. 2(b), with the average energies of 70.3 MeV (72% FWHM energy spread) and 74 MeV (70% FWHM energy spread) for the linearly and circularly polarized cases, respectively.

A tape system equipped with 100- μm -thickness polyethylene terephthalate (PET) film is placed near the exit of the gas jet, thus a plasma mirror is formed when the drive laser hits the PET film. The residual laser reflected by the plasma mirror then collides with the LWFA electron beam to generate AOCS x-ray photons. It should be noted that the normal of the tape has a slight angle (about 3°) with the incident laser to avoid the damage to the upstream optical components caused by the reflected lasers. Since the laser pulse preserves its polarization state during both the LWFA process and the nearly 180° reflection, the AOCS x rays near the axis maintain the same polarization state with the drive laser. Therefore, polarization-tunable x rays can

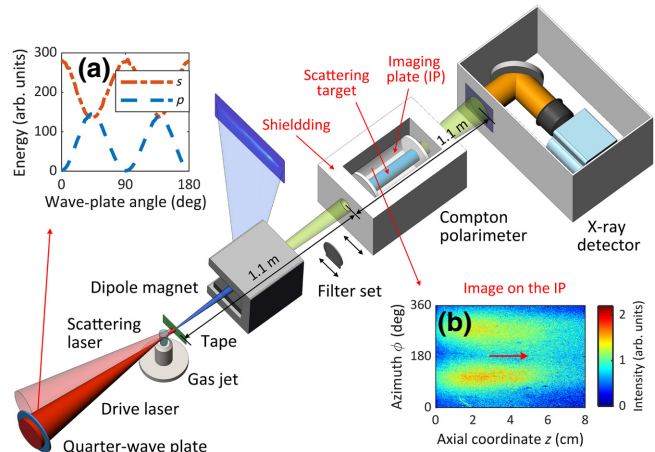


FIG. 1. Schematic layout of the experiment, where the filter set and the Compton polarimeter are both movable. (a) Laser energy of the *s*- and *p*-polarized components at different wave-plate angles, showing that the drive laser is linearly and circularly polarized at 0/45°, and elliptically polarized between 0° to 45°. (b) The two-dimensional azimuthal distribution of the secondary Compton scattering photons detected by the imaging plate in the Compton polarimeter, where the red arrow shows the propagation direction of the incident AOCS x rays.

be achieved by straightforwardly adjusting the polarization of the drive laser. The generated AOCS x rays are detected by a calibrated CsI(Tl) scintillation screen (Hamamatsu J8734) imaged onto an EMCCD (ANDOR DU888E), as shown in Fig. 1. Figures 3(a) and 3(b) are the accumulated x-ray profiles of 50-shot linearly and circularly polarized AOCS pulses, showing that their FWHM divergences are approximately 37/33 mrad (horizontal and vertical) and 29/28 mrad, respectively.

The photon energy of AOCS x rays near the axis can be described as $E_X = 4\gamma^2 E_L / (1 + a_0^2/2)$ [26], where γ is the Lorentz factor of the LWFA electron beam, E_L and a_0 are the photon energy and the peak-normalized vector potential of the scattering laser. Due to the energy spread of electron beams and the bandwidth of scattering lasers, the AOCS x rays will also have certain bandwidth. In the experiment, the x-ray spectrum is measured by an attenuation method based on the correlation between the x-ray attenuation coefficient and the x-ray photon energy [31,32]. A filter set made of copper and aluminum is adopted as the x-ray attenuator, where the copper filters are mainly sensitive for the high-energy x rays and the aluminum filters are mainly sensitive for the low-energy x rays. Generally, the spatial distribution of the AOCS x rays is axially symmetric around the x-ray path, thus our filter set is designed to be a group of concentric fans as shown in Fig. 3(e), where the corresponding serial number and thickness are marked on each filter. The attenuated x-ray profiles by the filter set for continuous 50-shot linearly and circularly polarized AOCS are shown in Figs. 3(c) and 3(d), respectively. Since the attenuated profiles near the

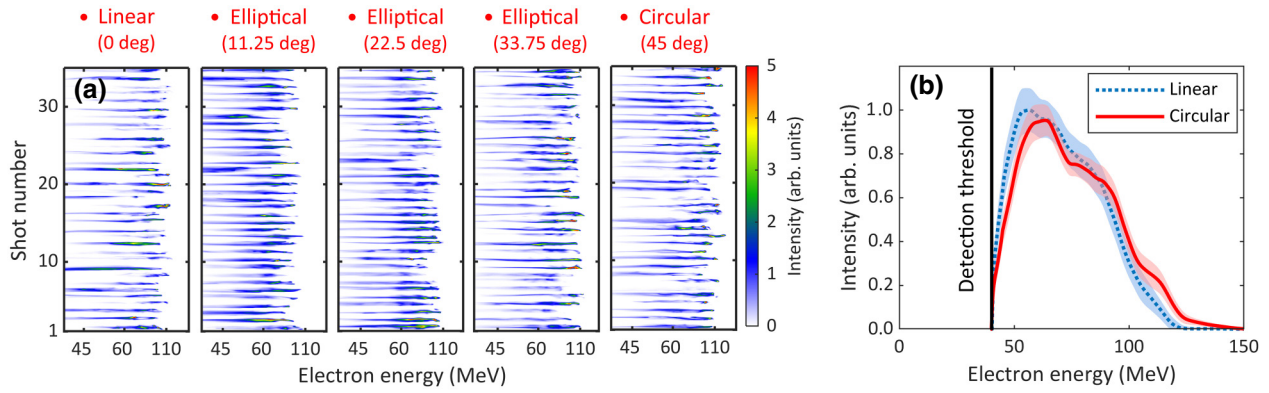


FIG. 2. The electron spectra driven by different polarized lasers. (a) Single-shot spectra for continuous 35-shot LWFA electron beams driven by different polarized lasers, where the wave-plate angle for each drive laser is labeled on the top. (b) 50-shot accumulated spectrum curves of the electron beams driven by the linearly and circularly polarized lasers, where the shaded areas around the curves are the FWHM errors. The detection threshold (40.3 MeV) is highlighted by a black solid line.

center of the filter set have relatively large noise, the normalized x-ray intensities at 4.5 mrad away from the AOCS axis are calculated, as shown in Fig. 3(f). The errors of the attenuated intensities are mainly caused by the noise in the x-ray profiles and the alignment error of the filter set with the AOCS axis (approximately 2 mrad for 50-shot AOCS pulse accumulation). The x-ray spectra are then reconstructed by the expectation-maximization (EM) algorithm [33], as shown in Figs. 3(g) and 3(h), where the spectral errors are determined by tens of reconstructions considering the errors of the attenuated x-ray intensities. It should be noted that there is no assumed spectral distribution in the reconstruction process. It can be calculated that the linearly polarized AOCS x rays have the average photon energy of $60(\pm 5)$ keV, the peak photon energy of 36 keV, and the FWHM bandwidth of 51 keV; the circularly polarized AOCS x rays have the average photon energy of $64(\pm 3)$ keV, the peak photon energy of 40 keV, and the FWHM bandwidth of 61 keV. According to the x-ray spectra and the x-ray detection efficiency, the single-shot photon yields of the linearly and circularly polarized AOCS are estimated to be approximately 1.1×10^7 and 1.3×10^7 using the x-ray profiles in Figs. 3(a) and 3(b).

III. POLARIZATION MEASUREMENT

To diagnose the polarization states of the AOCS x rays, a Compton polarimeter [27–29] is designed according to the x-ray parameters measured above. The differential cross section $d\sigma/d\Omega$ of Compton scattering can be described as

$$\frac{d\sigma}{d\Omega} = \frac{r_e^2 E_S^2}{2 E_0^2} \left(\frac{E_S}{E_0} + \frac{E_0}{E_S} - 2 \sin^2 \theta \frac{\cos^2 \phi + a \sin^2 \phi}{a + 1} \right), \quad (1)$$

where r_e is the classical electron radius, E_0 and E_S are the photon energy of the incident x rays and the secondary

Compton scattering x rays, θ is the forward scattering angle, ϕ is the azimuthal scattering angle, and a is related to the polarization states of the incident x rays ($a = 0$ and $a \rightarrow \infty$ for horizontal and vertical linear polarization, $a = 1$ for circular polarization). Equation (1) shows that the azimuthal distribution ($\theta = \pi/2$) of the secondary Compton photons is $\cos^2 \phi$ -like (or $\sin^2 \phi$ -like) for the linearly polarized incident x rays, while uniform for the circularly polarized incident x rays. Therefore, the azimuthal distribution of the secondary Compton photons can be used to identify different x-ray polarization states. Moreover, the polarization degree of the linearly polarized x rays can be obtained by analysing the peak-valley modulation of the $\cos^2 \phi$ -like (or $\sin^2 \phi$ -like) distribution.

The Compton polarimeter is composed of a scattering target, an imaging plate (IP), and a shielding system, as shown in Fig. 1. Similar polarimeter designs have been reported by Chattopadhyay *et al.* [28] and Zhang *et al.* [29]. To improve the secondary Compton photon yield and reduce the self-absorption, a polyethylene cylinder is chosen to be the scattering target due to its high Compton-scattering cross section ($0.186 \text{ cm}^2/\text{g}$ for 60-keV x-ray photons) and low density (0.96 g/cm^3). Considering the x-ray photon energy of about 60 keV, divergence of about 30 mrad, and drift distance of 1.1 m for our AOCS, the scattering target is designed to have 2-cm diameter (corresponding to 18.2-mrad acceptance divergence for the incident x rays) and 10-cm length (attenuated to 15% for 60-keV incident x rays). When the polarized x rays pass through the scattering target along its axis, the secondary Compton photons will be generated and their azimuthal distributions are detected by an IP rolled around the scattering target. Specifically, there is one 1-cm-thickness aluminum tray at each end of the scattering target to mount the IP, thus the effective detection length is 8 cm in the axial direction of the scattering target. A shielding system composed of an inner layer of 5-cm-thickness polyethylene and an outer

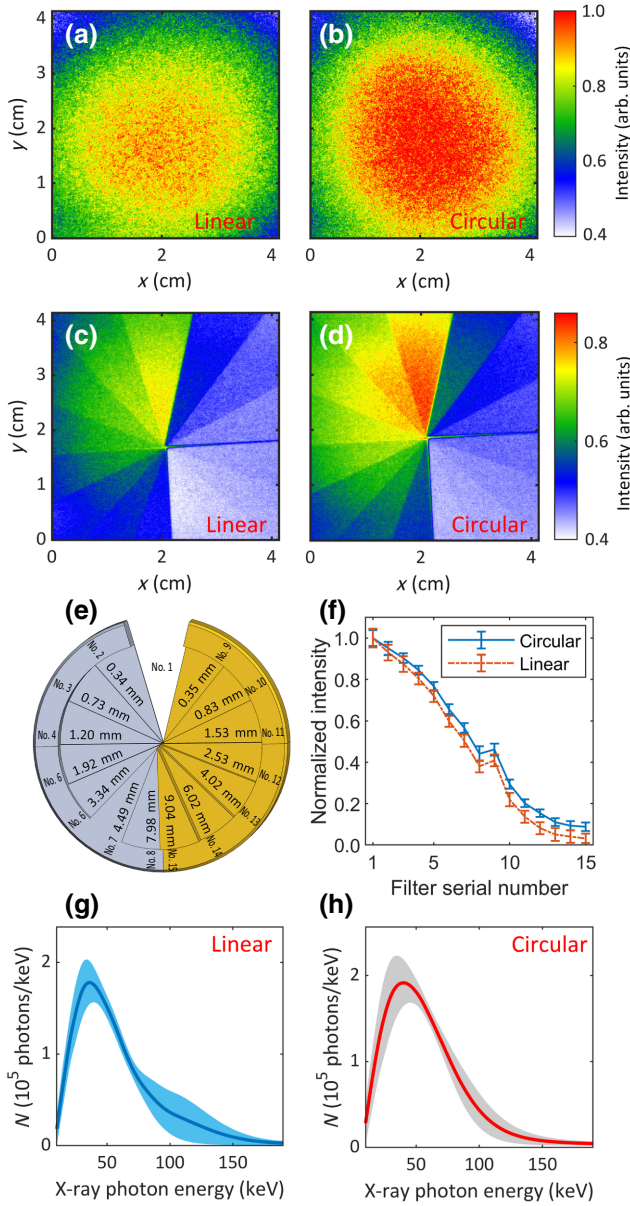


FIG. 3. The x-ray spectrum measurement results. (a) and (b) are the accumulated x-ray profiles of 50-shot linearly and circularly polarized AOCS pulses on the x-ray detector, while (c),(d) are those attenuated by the filter set. (e) is the structure of the filter set, where the yellow filters are made of copper and others are made of aluminum. The corresponding serial number and thickness are marked on each filter. (f) is the normalized x-ray intensities attenuated by the filter set. (g),(h) are the reconstructed spectra of the linearly and circularly polarized AOCS x rays, where the shaded areas around the two curves are the reconstruction errors.

layer of 10-cm-thickness lead encloses the scattering target and the IP, with a 2-cm-diameter hole in the front end to collimate the x rays.

To test this Compton polarimeter, a series of Monte Carlo simulations using the same polarimeter structure are

carried out by FLUKA [34]. The x rays are set to have the same spectra and divergences as the experimentally measured results, and only the x-ray polarization states and the off-axis deviations between the x-ray path and the axis of the scattering target are changed. It should be noted that the linearly polarized x rays mentioned in this paper are horizontally polarized throughout. The first three simulations are performed using 100% linearly polarized incident x rays with off-axis deviations of 0 mm (pass along the axis of the scattering target), 8 mm in the vertical direction (perpendicular to the x-ray polarization direction), and 8 mm in the horizontal direction (parallel to the x-ray polarization direction). The two-dimensional azimuthal distributions of the secondary Compton photons on the IP for these three simulations are shown in Figs. 4(a)–4(c). The corresponding one-dimensional distributions (the axial integration of the two-dimensional distributions) are plotted in Fig. 4(g), where the curves are all $\cos^2 \phi$ -like distributions, agreeing well with the theoretical prediction. It can be seen that the azimuthal distributions of the secondary Compton photons in Figs. 4(b) and 4(c) are both asymmetrical [peak values in the vertical direction are different for Fig. 4(b), and valley values in the horizontal direction are different for Fig. 4(c)], which are mainly caused by the off-axis deviations that more secondary Compton photons will be generated on the side the x-ray pulses bias. Taking I_p and I_v as the mean of the two peaks and the two valleys in the $\cos^2 \phi$ -like curves, the peak-valley modulation coefficient $\Lambda = (I_p - I_v)/(I_p + I_v)$ of these three cases are all calculated to be 38.8%, irrelevant to the off-axis deviations. Figure 4(d) is the two-dimensional azimuthal distribution of the secondary Compton photons using 50% linearly polarized incident x rays with 0-mm off-axis deviation, and the corresponding one-dimensional distribution is plotted in Fig. 4(g). Λ of this simulation is calculated to be 19.4%, which is half of that when the incident x rays are 100% linearly polarized, proving that Λ is proportional to the polarization degree of the linearly polarized incident x rays. Therefore, Λ can be used to calculate the polarization degree of the linearly polarized x rays. Figures 4(e) and 4(f) are the two-dimensional azimuthal distributions of the secondary Compton photons using 100% circularly polarized incident x rays with 0- and 8-mm off-axis deviations, and the corresponding one-dimensional distributions are plotted in Fig. 4(g). It can be seen that the azimuthal distribution of the secondary Compton photons is uniform when the circularly polarized x rays pass along the axis of the scattering target, while this distribution becomes asymmetrical when the x rays pass off axis with the scattering target, which is consistent with the theoretical prediction. According to the above simulations, it can be concluded that the x-ray polarization state can be well diagnosed by this Compton polarimeter.

According to the x-ray parameters and the Compton polarimeter structure, it can be estimated that there are

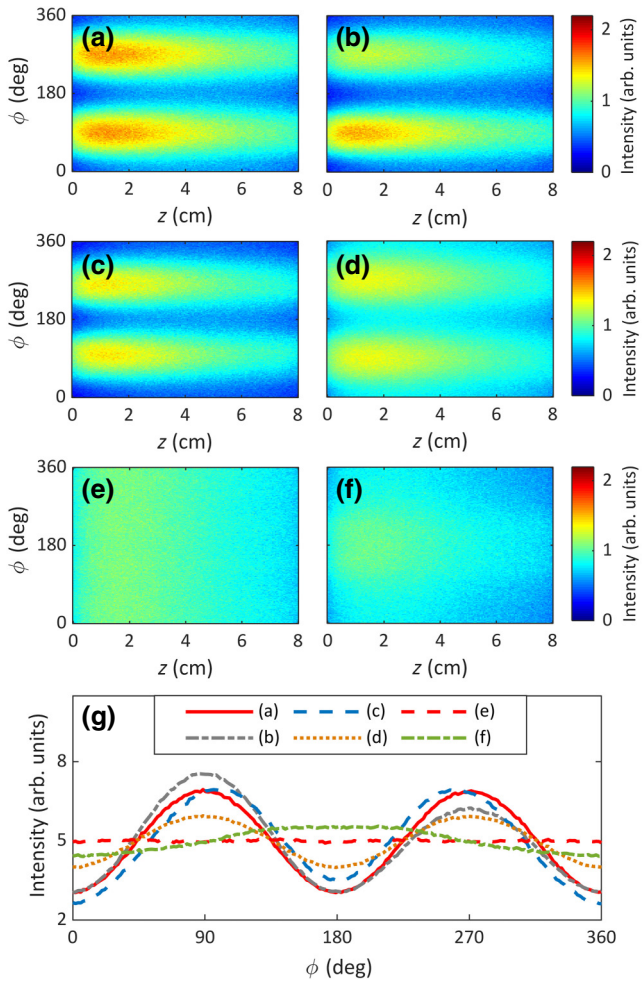


FIG. 4. Monte Carlo simulation results of the polarization diagnosis using the Compton polarimeter. (a)–(f) are the two-dimensional azimuthal distributions of the secondary Compton photons for the linearly and circularly polarized AOCS x rays, and the corresponding one-dimensional distributions are plotted in (g). In these simulations, (a)–(c) are performed using 100% linearly polarized incident x rays with different off-axis deviations (0 mm, 8 mm in the vertical direction, and 8 mm in the horizontal direction) between the x-ray path and the axis of the scattering target; (d) is performed using 50% linearly polarized incident x rays with 0-mm off-axis deviation; (e) and (f) are performed using 100% circularly polarized incident x rays with 0- and 8-mm off-axis deviations.

about 7×10^6 secondary Compton photons generated in the polyethylene scattering target for each AOCS pulse, and each pixel on the IP (the IP is scanned with $50 \mu\text{m}$ spatial resolution) can receive only $1 \sim 2$ Compton photons on average. Therefore, hundreds-of-shots accumulation is needed to ensure high SNR ratio of the IP image. In the experiment, considering that the repetition rate of our AOCS is 0.2 Hz (mainly limited by the vacuum system), continuous 600-shot AOCS pulses are performed within 50 min for each measurement, and the SNR ratio of the IP image is about 4. Figures 5(a) and 5(b) are

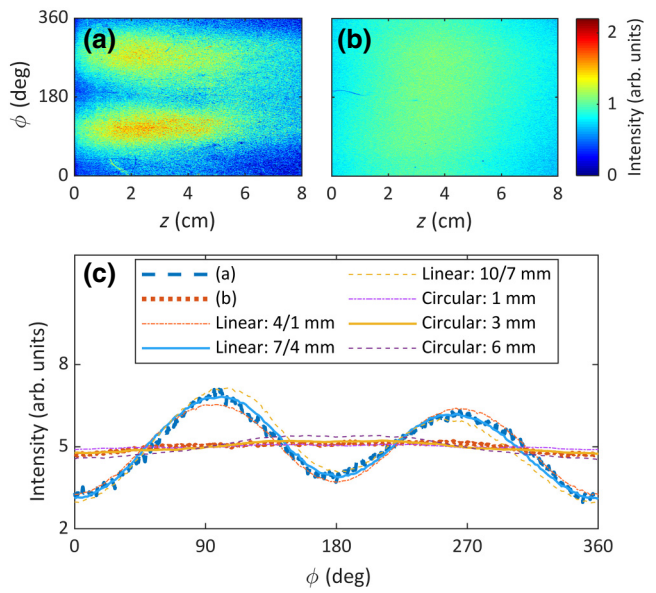


FIG. 5. Experiment results of the polarization diagnosis using the Compton polarimeter. (a),(b) are the two-dimensional azimuthal distributions of the secondary Compton photons for the linearly and circularly polarized AOCS x rays, and the corresponding one-dimensional distributions along with the simulated fitting curves are plotted in (c). The off-axis deviations of the linearly and circularly polarized fitting cases are marked in the legends.

the two-dimensional azimuthal distributions of the secondary Compton photons on the IP for the linearly and circularly polarized AOCS x rays, and the corresponding one-dimensional distribution curves are plotted in Fig. 5(c). Both the $\cos^2 \phi$ -like azimuthal distribution for the linearly polarized AOCS and the uniform azimuthal distribution for the circularly polarized AOCS are evident in the curves, verifying the polarization tunability of AOCS. The peak-valley modulation coefficient Λ of the linearly polarized AOCS is calculated to be $29.1(\pm 1.2)\%$ (the error is caused by the noise in the IP image), thus its polarization degree is determined to be $75(\pm 3)\%$ by comparing the Λ value with that of the 100% linearly polarized simulation case (38.8%). To estimate the off-axis deviations, a series of FLUKA simulations are performed using 75% linearly polarized and 100% circularly polarized incident x rays with different off-axis deviations to fit the experiment curves. It should be noted that the polarization degree of circularly polarized incident x rays does not affect the azimuthal distribution of the secondary Compton photons. The one-dimensional fitting curves are plotted in Fig. 5(c), indicating that the off-axis deviations are approximately $7/4$ mm (horizontal and vertical) for the linearly polarized AOCS x rays, and approximately 3 mm (absolute distance from the axis of the scattering target) for the circularly polarized AOCS x rays.

For a single electron colliding with a laser pulse (whether linearly or circularly polarized), the average polarization degree of the generated AOCS x rays decreases as the x-ray divergence increases, and the on-axis x rays (the AOCS axis is along the electron propagation direction) have the highest polarization degree up to 100% [15]. For a real electron beam with certain divergence, the AOCS x-ray pulses are the accumulation of the x rays generated by single electrons with different propagation directions, thus the average polarization degree of the x-ray pulses near the AOCS axis will decrease. To study the effect of electron divergence on AOCS polarization, Monte Carlo simulations about the generation of linearly and circularly polarized AOCS are carried out by CAIN [35]. The first two simulations are performed using the experiment conditions, where the electron-beam parameters are set as the LWFA electron beams driven by the linearly and circularly polarized lasers introduced in Sec. II; the scattering lasers are set to be 100% linearly and 100% circularly polarized with peak power density of $2.86 \times 10^{18} \text{ W/cm}^2$ and wavelength of 900 nm. Here, the scattering laser parameters are estimated by particle-in-cell simulations considering the evolution of the drive laser in the LWFA process and the reflection by the plasma mirror [32,36]. The x-ray polarization degree is described by the Stokes parameters in CAIN [15]. In these two simulations, the two-dimensional polarization degree distributions of the AOCS x rays are shown in Figs. 6(a) and 6(b), where the acceptance divergence of the Compton polarimeter (18.2 mrad) is highlighted by the black dashed circles. The average polarization degrees of AOCS within different x-ray divergences are plotted in Fig. 6(c), showing that higher average polarization degree can be obtained within smaller x-ray divergence. It can be seen that the on-axis polarization degrees (the average polarization degree of the x rays within 2-mrad divergence) of the linearly and circularly polarized AOCS are approximately 81% and 63%, respectively. Moreover, The average polarization degree of the linearly polarized AOCS within the acceptance divergence of the Compton polarimeter is 76%, agreeing well with the measurement result of $75(\pm 3)\%$. A series of CAIN simulations are then performed with different electron divergences (0.1-, 1-, 3-, 5-, 7-, 9-, 11-, 15-, 20-, 30-mrad FWHM), while other parameters in these simulations are the same as the first two simulations. The on-axis polarization degrees of the AOCS x rays in these simulations are plotted in Fig. 6(d). For both the linearly and circularly polarized AOCS, $>90\%$ on-axis polarization degree can be achieved using $<7\text{-mrad}$ FWHM electron divergence, and $>99\%$ on-axis polarization degree can be achieved using $<1\text{-mrad}$ FWHM electron divergence, showing that the on-axis polarization degree of AOCS can be efficiently improved by reducing the electron divergence. Nowadays, high-quality LWFA electron beams with $<1\text{-mrad}$ FWHM divergence have been reported [37,38], thus AOCS with

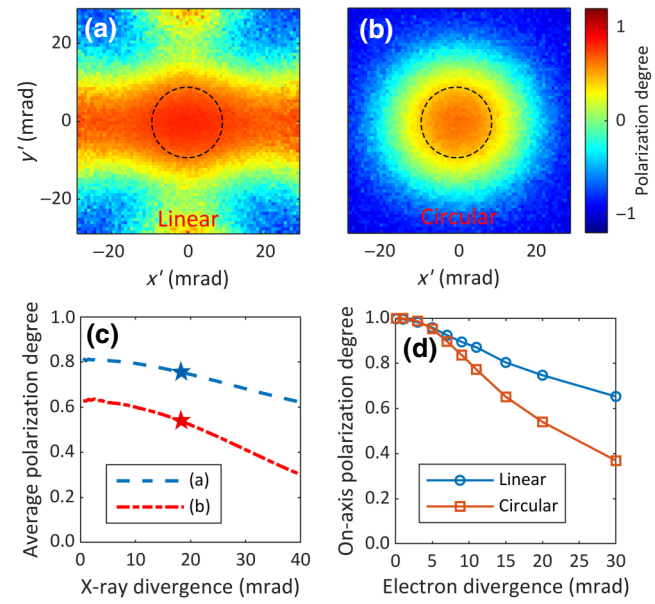


FIG. 6. Monte Carlo simulation results about the effect of electron divergence on AOCS polarization. (a) and (b) are the two-dimensional polarization degree distributions of the linearly and circularly polarized AOCS at the experiment conditions, where the black dashed circles indicate the acceptance divergence of the Compton polarimeter. (c) is the average polarization degrees within different x-ray divergences of (a) and (b), where the pentacles on the curves indicate the acceptance divergence of the Compton polarimeter. (d) is the on-axis polarization degrees of the AOCS x-rays generated using the electron beams with different FWHM divergences.

nearly 100% on-axis polarization degree can potentially be demonstrated in the near future.

IV. CONCLUSIONS

In this paper, the generation of about 60-keV polarization-tunable AOCS x rays using the plasma-mirror-based scheme is demonstrated, and the polarization states of the linearly and circularly polarized AOCS are diagnosed by a Compton polarimeter. The polarization state of AOCS is easily adjusted by tuning the polarization state of the drive laser using a quarter-wave plate, which is especially convenient and efficient for practical applications. The polarization degree of the linearly polarized AOCS x rays within 18.2 mrad is measured to be $75(\pm 3)\%$, which is consistent with the Monte Carlo simulation result. The polarization degree of both the linearly and circularly polarized AOCS can be further improved by optimizing the divergence of the LWFA electron beam. The repetition rate of our AOCS system is 0.2 Hz currently, which can be improved to 10–1000 Hz in the near future by upgrading the vacuum system [20,39]. This source can also generate >MeV polarization-tunable x rays by using

larger-scale laser system, which can significantly contribute to the high-energy applications such as the nuclear physics research.

ACKNOWLEDGMENTS

The authors thank Dr Yuchi Wu for the support of x-ray detection. This work is supported by the National Natural Science Foundation of China (Grant No. 11991071, No. 11875175 and No. 11991073) and Tsinghua University Initiative Scientific Research Program.

-
- [1] J. Christoffersson and S. Mattsson, Polarised x-rays in XRF-analysis for improved in vivo detectability of cadmium in man, *Phys. Med. Biol.* **28**, 1135 (1983).
- [2] M. J. Pushie, I. J. Pickering, M. Korbas, M. J. Hackett, and G. N. George, Elemental and chemically specific x-ray fluorescence imaging of biological systems, *Chem. Rev.* **114**, 8499 (2014).
- [3] J. Stöhr, Y. Wu, B. Hermsmeier, M. Samant, G. Harp, S. Koranda, D. Dunham, and B. Tonner, Element-specific magnetic microscopy with circularly polarized x-rays, *Science* **259**, 658 (1993).
- [4] M. Suzuki, H. Yumoto, T. Koyama, H. Yamazaki, T. Takeuchi, N. Kawamura, M. Mizumaki, H. Osawa, Y. Kondo, and J. Ariake, Magnetic microscopy using a circularly polarized hard-x-ray nanoprobe at SPRING-8, *Synchrotron Radiat. News* **33**, 4 (2020).
- [5] F. Bauwens, J. Bryssinck, D. De Frenne, K. Govaert, L. Govor, M. Hagemann, J. Heyse, E. Jacobs, W. Mondelaers, and V. Y. Ponomarev, Dipole transitions to bound states in Fe-56 and Ni-58, *Phys. Rev., C. Nucl. Phys.* **62**, 024302 (2000).
- [6] K. Govaert, W. Mondelaers, E. Jacobs, D. Defrenne, K. Persyn, S. Pomme, M. L. Yoneama, S. Lindenstruth, K. Huber, A. Jung, B. Starck, R. Stock, C. Wesselborg, R. D. Heil, U. Kneissl, and H. H. Pitz, Polarized bremsstrahlung nuclear-resonance fluorescence set-up at the 15 MeV linac in Gent, *Nucl. Instrum. Methods Phys. Res., Sect. A* **337**, 265 (1994).
- [7] J. W. Freeland, J. C. Lang, G. Srajer, R. Winarski, D. Shu, and D. M. Mills, A unique polarized x-ray facility at the advanced photon source, *Rev. Sci. Instrum.* **73**, 1408 (2002).
- [8] S. Yamamoto, T. Shioya, S. Sasaki, and H. Kitamura, Construction of insertion devices for elliptically polarized synchrotron radiation, *Rev. Sci. Instrum.* **60**, 1834 (1989).
- [9] A. A. Lutman, J. P. MacArthur, M. Ilchen, A. O. Lindahl, J. Buck, R. N. Coffee, G. L. Dakovski, L. Dammann, Y. Ding, and H. A. Dürr, Polarization control in an x-ray free-electron laser, *Nat. Photonics* **10**, 468 (2016).
- [10] E. Schneidmiller and M. Yurkov, Obtaining high degree of circular polarization at x-ray free electron lasers via a reverse undulator taper, *Phys. Rev. Spec. Top.-Accel. Beams* **16**, 110702 (2013).
- [11] J. Motz and R. Placious, Bremsstrahlung linear polarization, *Il Nuovo Cimento (1955–1965)* **15**, 571 (1960).
- [12] P. A. Ali, A. F. Al-Hussany, C. A. Bennett, D. A. Hancock, and A. M. El-Sharkawi, Plane polarized x-ray fluorescence system for the in vivo measurement of platinum in head and neck tumours, *Phys. Med. Biol.* **43**, 2337 (1998).
- [13] M. Goldhaber, L. Grodzins, and A. Sunyar, Evidence for circular polarization of bremsstrahlung produced by beta rays, *Phys. Rev.* **106**, 826 (1957).
- [14] S. Kashiwagi, M. Washio, T. Kobuki, R. Kuroda, I. Ben-Zvi, I. Pogorelsky, K. Kusche, J. Skaritka, V. Yakimenko, and X. J. Wang, Observation of high-intensity x-rays in inverse Compton scattering experiment, *Nucl. Instrum. Methods Phys. Res.* **455**, 36 (2000).
- [15] V. Petrillo, A. Bacci, C. Curatolo, I. Drebot, A. Giribono, C. Maroli, A. R. Rossi, L. Serafini, P. Tomassini, C. Vacca, and A. Variola, Polarization of x-gamma radiation produced by a Thomson and Compton inverse scattering, *Phys. Rev. Spec. Top.-Accel. Beams* **18**, 110701 (2015).
- [16] Y. Taira, T. Hayakawa, and M. Katoh, Gamma-ray vortices from nonlinear inverse Thomson scattering of circularly polarized light, *Sci. Rep.* **7**, 5018 (2017).
- [17] T. Tajima and J. M. Dawson, Laser Electron Accelerator, *Phys. Rev. Lett.* **43**, 267 (1979).
- [18] E. Esarey, C. Schroeder, and W. Leemans, Physics of laser-driven plasma-based electron accelerators, *Rev. Mod. Phys.* **81**, 1229 (2009).
- [19] S. M. Hooker, Developments in laser-driven plasma accelerators, *Nat. Photonics* **7**, 775 (2013).
- [20] A. R. Maier, N. M. Delbos, T. Eichner, L. Hübner, S. Jalas, L. Jeppe, S. W. Jolly, M. Kirchen, V. Leroux, and P. Messner, *et al.*, Decoding Sources of Energy Variability in a Laser-Plasma Accelerator, *Phys. Rev. X* **10**, 031039 (2020).
- [21] W. Lu, M. Tzoufras, C. Joshi, F. S. Tsung, W. B. Mori, J. Vieira, R. A. Fonseca, and L. O. Silva, Generating multi-GeV electron bunches using single stage laser wakefield acceleration in a 3D nonlinear regime, *Phys. Rev. Spec. Top.-Accel. Beams* **10**, 061301 (2007).
- [22] H. Schwoerer, B. Liesfeld, H. P. Schlenvoigt, K. U. Amthor, and R. Sauerbrey, Thomson-Backscattered X Rays from Laser-Accelerated Electrons, *Phys. Rev. Lett.* **96**, 014802 (2006).
- [23] S. Chen, N. D. Powers, I. Ghebregziabher, C. M. Maharjan, C. Liu, G. Golovin, S. Banerjee, J. Zhang, N. Cunningham, and A. Moorti, MeV-Energy X Rays from Inverse Compton Scattering with Laser-Wakefield Accelerated Electrons, *Phys. Rev. Lett.* **110**, 155003 (2013).
- [24] N. D. Powers, I. Ghebregziabher, G. Golovin, C. Liu, S. Chen, S. Banerjee, J. Zhang, and D. P. Umstadter, Quasi-monoenergetic and tunable x-rays from a laser-driven Compton light source, *Nat. Photonics* **8**, 28 (2014).
- [25] K. T. Phuoc, S. Corde, C. Thaury, V. Malka, A. Tafzi, J. P. Goddet, R. C. Shah, S. Sebban, and A. Rousse, All-optical Compton gamma-ray source, *Nat. Photonics* **6**, 308 (2012).
- [26] A. Döpp, E. Guillaume, C. Thaury, J. Gautier, I. Andriyash, A. Lifschitz, V. Malka, A. Rousse, and K. T. Phuoc, An all-optical Compton source for single-exposure x-ray imaging, *Plasma Phys. Controlled Fusion* **58**, 034005 (2016).
- [27] T. Michel, J. Durst, and J. Jakubek, X-ray polarimetry by means of Compton scattering in the sensor of a hybrid photon counting pixel detector, *Nucl. Instrum. Methods Phys. Res. Section A* **603**, 384 (2009).
- [28] T. Chattopadhyay, S. V. Vadawale, and J. Pendharkar, Compton polarimeter as a focal plane detector for hard

- x-ray telescope: Sensitivity estimation with Geant4 simulations, *Exp. Astron.* **35**, 391 (2013).
- [29] H. Zhang, Y. Du, C. Tang, L. Yan, and W. Huang, Experimental polarization control of Thomson scattering x/gamma-ray source, Preprint [ArXiv:1612.09403](https://arxiv.org/abs/1612.09403) (2016).
- [30] H. Jian-Fei, Y. Li-Xin, P. Chih-Hao, Z. Chao-Jie, L. Fei, W. Yang, W. Yi-Peng, X. Xin-Lu, D. Ying-Chao, and H. Wen-Hui, Generating 10–40 MeV high quality monoenergetic electron beams using a 5 TW 60 fs laser at Tsinghua University, *Chin. Phys. C* **39**, 017001 (2015).
- [31] B. Guo, X. Zhang, J. Zhang, J. Hua, C.-H. Pai, C. Zhang, H.-H. Chu, W. Mori, C. Joshi, and J. Wang, High-resolution phase-contrast imaging of biological specimens using a stable betatron x-ray source in the multiple-exposure mode, *Sci. Rep.* **9**, 7796 (2019).
- [32] Y. Ma, J. Hua, D. Liu, Y. He, T. Zhang, J. Chen, F. Yang, X. Ning, Z. Yang, and J. Zhang, Region-of-interest micro-focus computed tomography based on an all-optical inverse Compton scattering source, *Matter Radiat. Extrem.* **5**, 064401 (2020).
- [33] T. K. Moon, The expectation-maximization algorithm, *IEEE Signal Process. Mag.* **13**, 47 (1996).
- [34] G. Battistoni, F. Cerutti, A. Fasso, A. Ferrari, S. Muraro, J. Ranft, S. Roesler, and P. Sala, in *AIP Conference Proceedings* (American Institute of Physics), p. 31, Vol. 896.
- [35] P. Chen, G. Horton-Smith, T. Ohgaki, A. Weidemann, and K. Yokoya, Cain: Conglomerat d'abel et d'interactions non-lineaires, *Nucl. Instrum. Methods Phys. Res. Section A* **355**, 107 (1995).
- [36] Z. Nie, C.-H. Pai, J. Hua, C. Zhang, Y. Wu, Y. Wan, F. Li, J. Zhang, Z. Cheng, and Q. Su, Relativistic single-cycle tunable infrared pulses generated from a tailored plasma density structure, *Nat. Photonics* **12**, 489 (2018).
- [37] W. T. Wang, W. T. Li, J. S. Liu, Z. J. Zhang, R. Qi, C. H. Yu, J. Q. Liu, M. Fang, Z. Y. Qin, C. Wang, Y. Xu, F. X. Wu, Y. X. Leng, R. X. Li, and Z. Z. Xu, High-Brightness High-Energy Electron Beams from a Laser Wakefield Accelerator via Energy Chirp Control, *Phys. Rev. Lett.* **117**, 124801 (2016).
- [38] L. T. Ke, K. Feng, W. T. Wang, Z. Y. Qin, C. H. Yu, Y. Wu, Y. Chen, R. Qi, Z. J. Zhang, Y. Xu, X. J. Yang, Y. X. Leng, J. S. Liu, R. X. Li, and Z. Z. Xu, Near-GeV Electron Beams at a Few Per-Mille Level from a Laser Wakefield Accelerator via Density-Tailored Plasma, *Phys. Rev. Lett.* **126**, 214801 (2021).
- [39] D. Guenot, D. Gustas, A. Vernier, B. Beaurepaire, F. Bohle, M. Bocoum, M. Lozano, A. Jullien, R. Lopez-Martens, A. Lifschitz, and J. Faure, Relativistic electron beams driven by kHz single-cycle light pulses, *Nat. Photonics* **11**, 293 (2017).